Meteorol Atmos Phys (2009) 105:191–210
DOI 10.1007/s00703-009-0044-5

ORIGINAL PAPER

Regional climate model simulation of the AMMA Special Observing Period #3 and the pre-Helene easterly wave

Leonard M. Druyan · Matthew Fulakeza · Patrick Lonergan · Erik Noble

Received: 6 April 2009 / Accepted: 21 August 2009 / Published online: 10 September 2009

Abstract The study examines results of dynamic downscaling of two global analyses: the National Center for Environmental Prediction/National Center for Atmospheric Research (NCEP/NCAR) reanalysis II and the Global Forecast System final analysis (FNL). Downscaling to a 0.5° grid over West Africa and the adjacent Atlantic Ocean is accomplished by each of two regional models, the Regional Model, version 3 (RM3) of the Center for Climate Systems Research and the Weather, Research and Forecasting model (WRF). Simulations are for September 2006, the African Monsoon Multidisciplinary Analysis (AMMA) Special Observing Period #3 (SOP-3). The aim of this study is to exploit the increased spatial detail in the simulations and representations of climate fields by the regional models to analyze meteorological systems within the SOP-3 area of interest and time frame. In particular, the paper focuses on the regional models' representations of the structure and movement of a prominent easterly wave during September 10–13th, the precursor of Tropical Storm/Hurricane Helene. It describes the RM3 simulated structure of the developing storm in terms of circulation, precipitation, vertical motion, cumulus heating rates, and cross-sections of wind and geopotential height anomalies. Simulated cumulus heating rates within the wave's main precipitation area imply a lowering of the bases of active cumulus in the transition from the African continent to the Atlantic, indicating that the ocean environment promotes greater upward latent heat flux that in turn intensifies overlying storms. RM3 circulation, precipitation patterns, and storm trajectory are reasonably consistent with observational evidence. Experiments show that precipitation rates near 6°N over the eastern North Atlantic are sensitive to vertical thermal stability, such that they are enhanced by warmer in situ sea-surface temperatures (SSTs) and diminished by colder SSTs. However, prescribing colder SST causes increases in precipitation north of 9°N within areas of large scale upward vertical motion where rainfall rates are less sensitive to in situ SSTs. The evaluation of WRF indicates that its storm propagation is too fast over West Africa, where associated WRF precipitation rates are exaggerated, but its performance is improved over the Atlantic.

L. M. Druyan (✉) · M. Fulakeza · P. Lonergan
NASA/Goddard Institute for Space Studies,
NYC and Center for Climate Systems Research,
Columbia University, New York, USA
e-mail: LDruyan@giss.nasa.gov; ld12@columbia.edu

E. Noble
University of Colorado, Boulder, CO, USA

1 Introduction

The African Monsoon Multidisciplinary Analysis (AMMA) is a concerted effort to improve our understanding of the climate of West Africa, especially the variability of precipitation systems (Redelsperger et al. 2006). The goal is for this increased understanding to improve techniques of seasonal prediction of rainfall anomalies, including droughts and floods, which have a devastating socio-economic impact on very vulnerable populations of the Sahel. In addition, there is special interest in studying disturbances entering the North Atlantic from West Africa, since they are often precursors of tropical storms. The NASA African Monsoon Multidisciplinary Analysis (NAMMA) contribution to the broader AMMA campaign focuses on the downstream or oceanic evolution of precipitating convective systems. To this end, NAMMA sponsored a field

research investigation based in the Cape Verde Islands, 350 miles off the coast of Senegal in West Africa during the AMMA Special Observation Period #3 (SOP-3), which was September 2006.

The AMMA SOP-3 employed extensive networks of ground-based and aircraft observations, supplemented by measurements from satellite-borne sensors. Although the SOP-3 successfully generated a considerable volume and variety of data, no field study can specify the complete space–time distribution of climate variables. One way to increase coverage is to use an atmospheric simulation model for time and space interpolation. For example, the National Center for Environmental Prediction reanalysis II (NCPR2) assimilates single point observations into a continuous global atmospheric model simulation (Kanamitsu et al. 2002). However, NCPR2 data are archived on a rather coarse grid of 2.5° latitude and longitude spacing. The present study evaluates simulated climate fields from two regional climate models that compute the climate evolution on finer grids of 0.5° spacing over a limited area that includes West Africa and the eastern Atlantic Ocean. It creates the data sets by dynamic downscaling of global analyses to the higher horizontal resolution. In particular, four-dimensional matrices of the time evolution of atmospheric conditions during SOP-3 are created, based on simulations from the Regional Model, version 3 (RM3) of the Center for Climate Systems Research (CCSR) and the Weather, Research and Forecasting model (WRF). Reed et al. (1988) and Thorncroft and Hodges (2001) deduced African easterly wave (AEW) trajectories over the eastern North Atlantic Ocean based on circulation data from global ECMWF analyses gridded at about 3° spacing. The present paper also considers AEW trajectories, albeit for a single month, but here the analysis is based on model integrations at higher resolution (0.5° grid).

The aim of this study is to exploit the increased spatial detail in the simulation and representation of climate fields by regional climate models to analyze meteorological systems within the SOP-3 area of interest and time frame. In particular, the paper focuses on the regional models' representation of the structure and movement of a prominent easterly wave and how it changes in the transition from continent to ocean. Schmidlin et al. (2007) show time-altitude cross-sections of SOP-3 radiosonde observed winds and humidity and radar echoes at Praia, Cape Verde (15°N, 23.5°W) as this storm traversed on September 12–13, 2006. The present study describes the regional model simulated structure of the developing storm in terms of circulation, precipitation, vertical motion, cumulus heating rates, and cross-sections of wind and geopotential height anomalies.

Via a series of simulation experiments, the study also examines the sensitivity of September 2006 precipitation over the eastern tropical North Atlantic Ocean, and especially the sensitivity of storm structure during September 12–13, to the magnitude of the tropical sea-surface temperature (SST) maximum. Chiang et al. (2002) determined the influence of SST gradients on monthly mean locations of Atlantic Ocean Inter-tropical convergence zone (ITCZ) moist convection. Since the monthly mean is composed of precipitation characteristics of many individual events, precipitation from traversing storms is presumably sensitive to SST anomalies via their impact on sensible and latent heat fluxes. The current investigation examines whether storm circulation and/or precipitation are altered by either cold or warm SST anomalies of the ocean surface below the storm in the eastern tropical North Atlantic Ocean.

Simulated data are compared with satellite-based estimates of precipitation rates, with reanalysis and, in one case, with SOP-3 TOGA (Tropical Ocean and Global Atmosphere) ground-based radar echoes and time-altitude cross-sections of radiosonde observed winds and humidity. Eventually, the analysis might be improved by four-dimensional assimilation of raw observations into the integrating model output, but this is beyond the scope of the current study.

Realistic downscaling requires a model capable of simulating important climate components, in this case, of the West African monsoon (WAM) and the adjacent eastern Atlantic Inter-tropical convergence zone (ITCZ). The RM3 performance for other summers was reported in previous publications (Druyan et al. 2006, 2008). A preliminary look at the performance of the WRF in simulating the WAM and eastern Atlantic ITCZ related climate features is presented here for the first time.

2 Models and experiments

Fritsch and Carbone (2004) noted serious deficiencies in the current technology of modeling moist convection that is used as the basis for warm-season quantitative precipitation forecasting. Nevertheless, the RM3, developed and run at CCSR, simulates time–space patterns of westward-propagating precipitation swaths that compare quite favorably with daily estimates from Tropical Rainfall Measurement Mission (TRMM) satellite data after an initial spin-up of about 6 days (Druyan and Fulakeza 2005; Druyan et al. 2006). These previous studies have documented how the RM3 simulates the important mesoscale and synoptic features of the WAM, including AEWs and the African Easterly Jet. The current paper shows examples from mesoscale four-dimensional data sets of evolving climate variables over West Africa and the adjacent Atlantic Ocean for the AMMA SOP-3, September 2006, from continuous

RM3 and WRF nested simulations on a grid with 0.5° spacing.

Druyan et al. (2006) described the important components of the newest, third-generation version RM3, so only a brief description is given here. It uses the same land surface (LS) process model that is used in the Goddard Institute for Space Studies global climate model (GCM) (Rosenzweig and Abramopoulos 1997; Hansen et al. 2002). The LS model consists of two integrated parts, the soil and the canopy, and it conserves water and heat while simulating their vertical fluxes. The RM3 modeled soil is divided into six layers to a depth of 3.5 m, and the model distinguishes between five textures of soil. The canopy, modeled as a separate layer located above the soil, is responsible for the interception of precipitation, evaporation of accumulated water, and removal of soil water through transpiration.

The Del Genio and Yao (1993) moist convection parameterization and the Del Genio et al. (1996) scheme for the effects of cloud liquid water have also been incorporated into the RM3. These are components originally developed for the Goddard Institute for Space Studies GCM, which itself has been extensively applied to climate sensitivity studies (e.g., Hansen et al. 2002). The cloud liquid water scheme allows for life cycle effects in stratiform clouds and permits cloud optical properties to be determined interactively.

Integrations of the RM3 are made at 28 vertical levels, within a domain extending from 20°S to 35°N and 35°W to 35°E, and on a grid with 0.5° spacing. The RM3 simulation was initialized with NCEP reanalysis II (NCPR2) (Kanamitsu et al. 2002) atmospheric conditions, sea-surface temperatures (SSTs), and soil moisture for August 15, 2006 at 00 UT. Lateral boundary conditions (LBCs) and SSTs to drive RM3 simulations are taken four times daily from NCPR2 global analyses. NCPR2 is based on data assimilation executed at an equivalent grid spacing of about 210 km, but data are archived on a 2.5° grid. In addition to this basic simulation (hereafter the control), three prescribed SST change experiments (described below) are initiated and analyzed.

The Weather Research and Forecasting model (WRF) is another regional weather and climate model, which was developed at the National Center for Atmospheric Research (NCAR). One WRF version is currently producing operational weather forecasts over North America. In light of the broad interest in other WRF applications within the scientific community, this very preliminary glimpse of WRF performance over West Africa and the adjacent Atlantic Ocean is included here against the background of RM3 results for the same case study.

LBCs and SSTs to drive WRF simulations are taken four times daily from FNL global analyses. FNL refers to the 1°×1° observational analysis used by the National Oceanic and Atmospheric Administration (NOAA) for initial conditions in the Global Forecast System (GFS), except that FNL contains additional late data. Results here use the WRF model release version 2.2.1 (November 2007) by NCAR, which at the time of the research provided modules for creating LBCs from GFS data (and not from NCPR2). Although FNL and NCPR2 purport to represent the same actual conditions, differences in LBCs supplied by the two data sets are probably responsible for some of the differences between RM3 and WRF simulation results.

The WRF simulation described here was initialized with FNL atmospheric conditions, SSTs, and soil moisture for August 1, 2006, at 00 UT and the simulation was run until September 30, 2006 over the same domain as the RM3. Regional model simulations presumably "forget" the initial conditions after about 10 days, so the longer spin-up compared to the RM3 design should not adversely affect WRF performance.

The physics options used for this WRF simulation include:

- Cloud microphysics scheme: WRF Single Moment (WSM) 3-class (Skamarock et al. 2005)
- Cumulus scheme: Kain-Fritch (Kain and Fritch 1993)
- Surface layer scheme: Monin–Obukhov similarity (Skamarock et al. 2005)
- Land-surface model: Noah 4-lyr (Chen and Dudhia 2001)
- Planetary boundary layer (PBL): Yonsei University (YSU PBL) (Skamarock et al. 2005)
- Rapid radiative transfer model (RRTM) for longwave (Mlawer et al. 1997)
- Goddard shortwave radiative transfer (Chou and Suarez 1994)

Other versions of WRF using alternative components were tried, but they gave less satisfactory results, which will be reported in future publications.

3 Overview

Figure 1 shows two Hovmöller time-longitude distributions for September 2006: (a) the meridional wind component at 700 mb (*v7*), four times per day, and (b) daily precipitation accumulations. Figure 1a agrees quite well with corresponding NCPR2 data and Fig. 1b with corresponding TRMM estimates (neither shown). The space–time correlation coefficient between the data shown in Fig. 1a and corresponding NCPR2 is 0.84 and between the data shown in Fig. 1b versus TRMM, 0.58. Alternating bands of negative and positive *v7* show the passage of transient easterly waves, and the diagonal pattern indicates westward

propagation. The trough of the 700 mb easterly wave disturbance featuring the heaviest daily precipitation accumulations crossed 10°E on September 7th, reached the coast on September 12th, and remained strong beyond its traversal of 30°W on September 14th. NOAA tracking indicates that Tropical Storm 'Helene' formed in the eastern tropical Atlantic Ocean on September 14th (Brown 2006). The location of the tropical depression at 12 UT on September 12th was 12°N, 22°W. Figure 1 shows that heavy precipitation propagated westward coinciding with the sector of northerly *v7* west of the moving trough line. Other westward propagating precipitation maxima are evident from the RM3 results and confirmed by TRMM estimates (not shown) and by the Schmidlin et al. (2007) analysis of Praia (Cape Verde, 15°N, 23.5°W) station data. An additional perspective is provided by our animation of the 925 mb reanalysis circulation with superimposed 3-hourly TRMM estimates for the entire September 2006 (http://wamme.geog.ucla.edu/simulations.html). Each diagonal precipitation swath in Fig. 1b can be matched to a corresponding pair of negative and positive *v7*, indicating that significant precipitation events are associated with transient easterly waves.

Figure 2a and b shows spectra of simulated *v7* time series for September 2006 at two selected grid locations. While both points are at the same latitude, Fig. 2a is representative of wave activity over the Atlantic coastal waters and Fig. 2b depicts continental activity (see Fig. 2c). In both locations significant peaks indicate periodicities of 3.3 and 4.3 days, typical of AEWs (Reed et al. 1988; Diedhiou et al. 1999). The spectrum loses about 25% of its peak amplitude at 4.3 days in the transition from 5°W to 22°W, but remains unchanged for 3.3-day period waves. Wavelet analysis (not shown) of the same data as represented by Fig. 2a, b also indicates lower spectral amplitudes over the ocean point with the maximum signifying 3.3-day periodicity. The wavelets, moreover, imply that each location experienced only one continuous interval of statistically significant periodic fluctuations of *v7*: September 5–16 over land and September 9–18 over the ocean. Figure 2c shows the spatial distribution of spectral amplitudes of *v7* time series averaged over 3–6-day periods. Two distinct maxima indicate the preferred trajectory of AEWs during September 2006. High spectral amplitudes along the Gulf of Guinea coast (near 5°N) are consistent with the path of

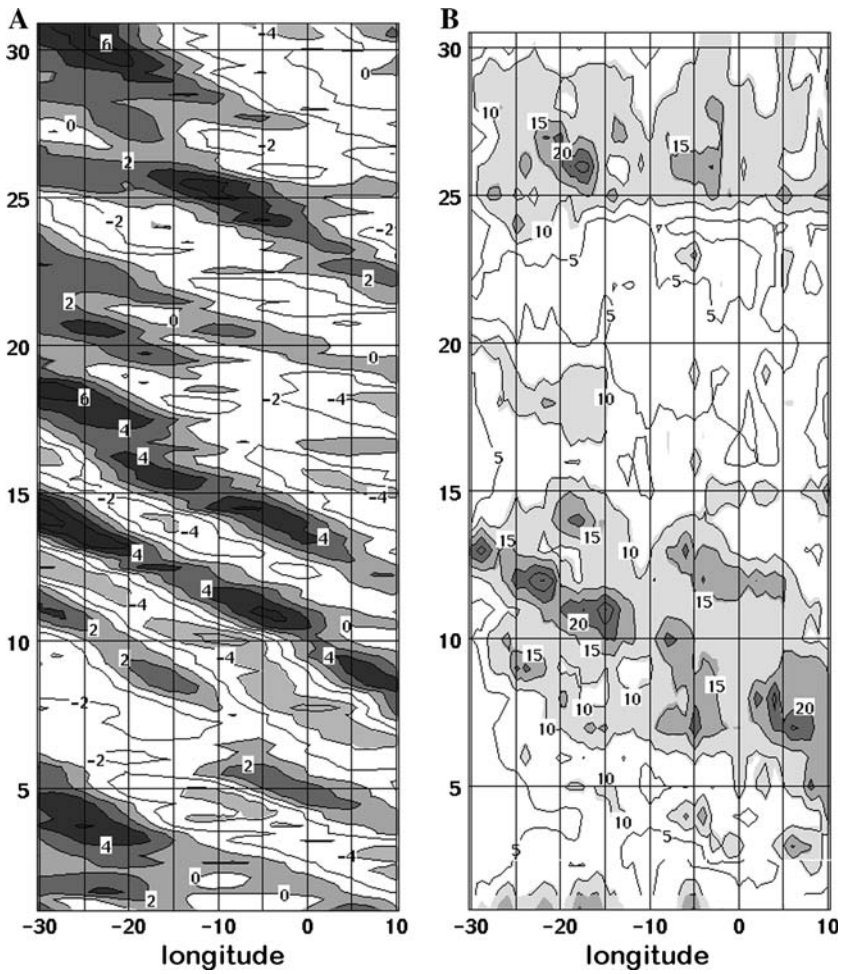

Fig. 1 Hovmöller time-longitude distribution of RM3 control simulation: **a** meridional wind component at 700 mb (m s^{-1}), 4× per day; **b** daily precipitation accumulation (mm), for September 1–30, averaged between 5 and 15°N

the pre- Helene wave, as discussed below. The second trajectory of AEWs is along 15°N over the eastern Atlantic Ocean, where results imply that 3–6-day period waves grow stronger as they propagate out over the Atlantic. This contrasts with east to west decreases of 3–6-day spectral amplitude at lower latitudes, such as those represented by the spectra at 10°N, shown in Fig. 2a, b. The maximum spectral amplitudes shown in Fig. 2c for September 2006 are between 30 and 60% stronger than those previously shown for RM3 simulations for June–September forced with 2003 NCEP/NCAR Reanalysis I data (Druyan et al. 2008).

Zones of maximum vorticity variance also detect trajectories of transient cyclonic disturbances. For example, Reed et al. (1988) deduced AEW trajectories based on gridded data from ECMWF analyses and forecasts projected on a 3° by 3° latitude–longitude grid by mapping the 700 mb vorticity variance filtered for 2.9–4.0 and 2.9–4.7-day periods. Their analysis was confined to August–September 1985 and their Fig. 4 showed northerly and southerly AEW tracks merging into one along 19°N over the eastern North Atlantic Ocean. The spatial distribution of 700 mb vorticity variance filtered for 3–6-day periods in the current September 2006 simulation (not shown) indicated the same two AEW trajectories as the distribution of spectral amplitudes shown in Fig. 2c. Thorncroft and Hodges (2001) tracked AEW vorticity maxima at 600 and 850 mb over West Africa and the Atlantic Ocean using 20 years of ECMWF analyses with an equivalent horizontal grid of 2.8°. They detected AEW trajectories along 10–13°N, but their data refer to the entire summer, while results here refer to a single September (and are based on 700 mb circulation). Thorncroft and Hodges (2001) as well as Druyan et al. (2006) emphasized that there is considerable interannual variability in AEW tracks associated with the WAM.

4 The storm of September 10–12, 2006

4.1 Circulation and precipitation

The pre-Helene African easterly wave disturbance crossed the African Atlantic coast on September 11–12th. It developed into a tropical depression on September 12th, into Tropical Storm Helene on September 14th and into Hurricane Helene on September 16th (see Brown 2006). Its movement and structure during the segment September 10–13 over West Africa and the eastern tropical Atlantic are next examined. Figure 3a shows the NCPR2 streamlines at 925 mb for 00 UT on September 10, 2006, which depict a cyclonic center over 14°N, 5°W. The RM3 center of cyclonic circulation at 925 mb (Fig. 3b) is slightly south of the NCPR2 position, probably owing to this model's higher resolution. The disturbance causes lower tropospheric convergence over much of West Africa, including a

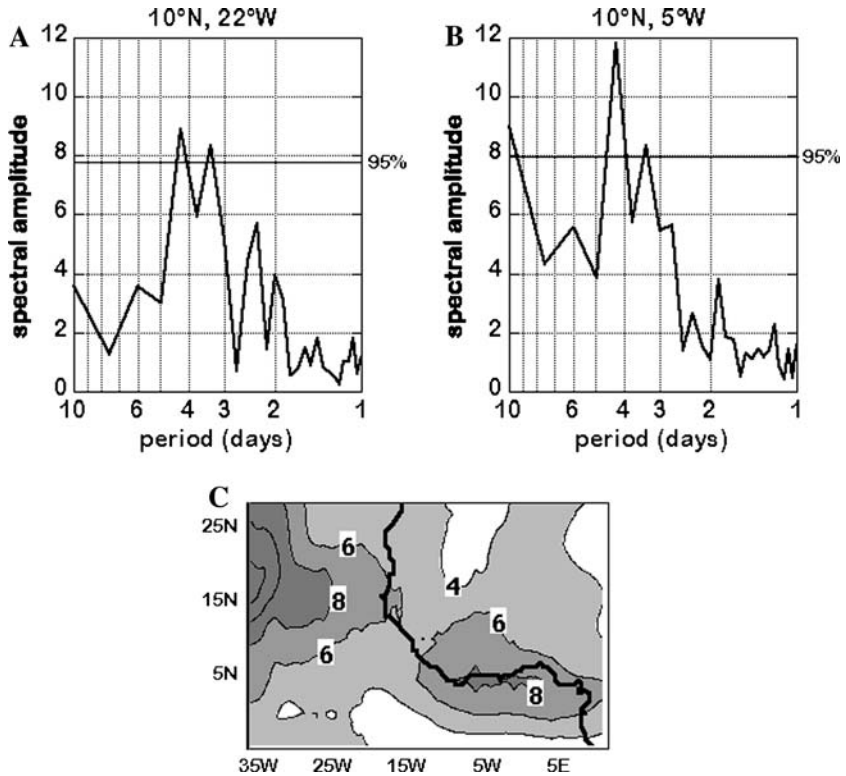

Fig. 2 Spectra of RM3 simulated 700 mb meridional wind (*v7*) time series four times per day, September 1–30, 2006 at each of two grid locations: **a** 10°N, 22°W, **b** 10°N, 5°W (the threshold for 95% statistical significance is indicated), and **c** spatial distribution of average spectral amplitudes for 3–6 day periods of the same *v7* time series, but at all points

southwesterly monsoon flow from the Gulf of Guinea coast to the Sahel. It is associated with an easterly wave in the 700 mb circulation (Fig. 3c) with its trough oriented northeast–southwest and passing through 11°N, 0°.

Figure 4a, b, c shows the accumulated precipitation for September 10, 2006, respectively, for the RM3, TRMM estimates, and the Famine Early Warning System (FEWS) data, which incorporate rain gauge measurements as well as satellite radiometric observations. The RM3 and TRMM representations indicate a circular rainfall maximum that overlaps the center of cyclonic circulation shown in Fig. 3b, but the heaviest precipitation is displaced to the southwest toward the moist monsoon air mass. This RM3 maximum is about 45 mm while the corresponding TRMM maximum exceeds 70 mm. The circular shape of the area of heavy rainfall suggests a mesoscale convective complex (MCC). RM3 and TRMM show the same pattern of rainfall distribution, although they are not in agreement about absolute values. The RM3 simulates lower maxima, but more extensive areas of light rain. The corresponding FEWS distribution (Fig. 4c) also indicates a broad area of light rain, with a maximum of about 50 mm. A low frequency of rain-free events over West Africa during the summer monsoon is a documented shortcoming of the RM3 (Druyan et al. 2006) and probably a deficiency of the moist convection scheme.

By 00 UT on September 11, the 925 mb vortex (Fig. 5a) and the 700 mb trough (Fig. 5b) have advanced westward about 8°. The near-surface confluence, and presumably the convergence, southwest of the vortex center has sharpened considerably and it now extends westward along 8–10°N out over the coastal waters to about 25°W. Accordingly, the precipitation accumulations for September 11 show a transition from the previous day (compare Fig. 4a to Fig. 5c). In particular, the remnant of the MCC has moved in tandem with the vortex center to 13°N, 14°W, but it has weakened. Heavy precipitation has broken out along the near-surface convergence at 8°N over the coastal waters. The RM3, TRMM (not shown), and FEWS (not shown) all indicate the same two precipitation maxima.

The near-surface vortex is at 12°N, 20°W by 00 UT on September 12th (Fig. 6a) and has therefore shifted southward some 2°, but its zonal movement has slowed, allowing the upper trough to almost catch up. NCPR2 locates the 925 mb vortex center at 12.5°N, 20°W (not shown). The rather slow moving 700 mb trough flattens somewhat and reaches the Atlantic coast (Fig. 6b). Figure 7 shows that the 8°N surface convergence zone still experiences heavy precipitation. In addition, a large comma shaped area of heavy precipitation has developed near 21°W coinciding with the low-level cyclonic vortex and just west of the 700 mb trough. TRMM estimates of

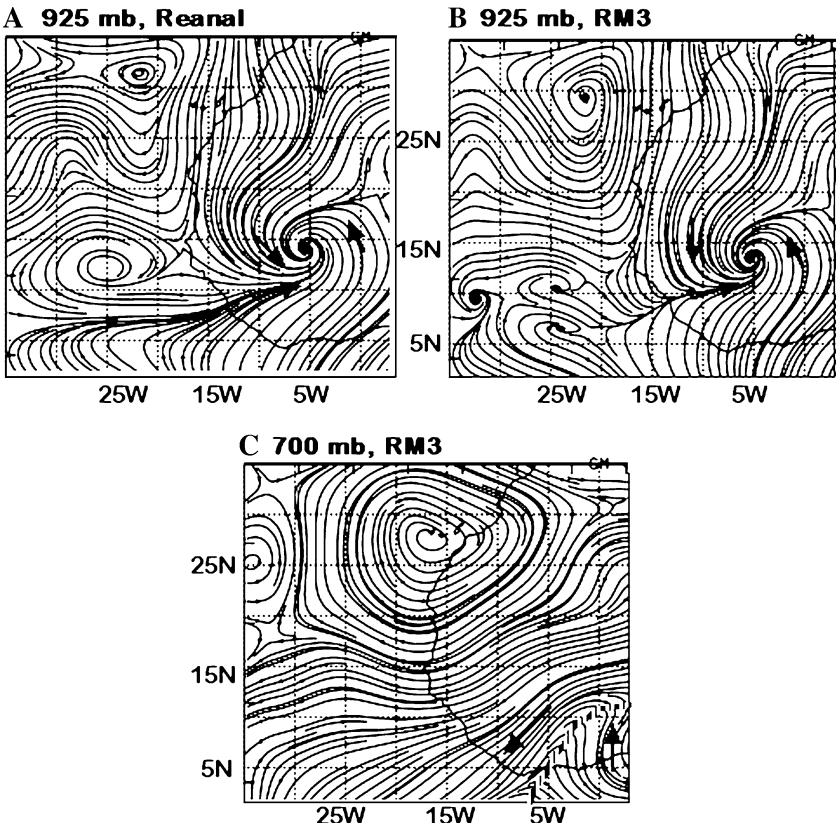

Fig. 3 Circulation at 00 UT on September 10, 2006: **a** NCEP reanalysis II 925 mb streamlines (Courtesy NOAA/ERSL), **b** RM3 simulated 925 mb streamlines, and **c** RM3 simulated 700 mb streamlines

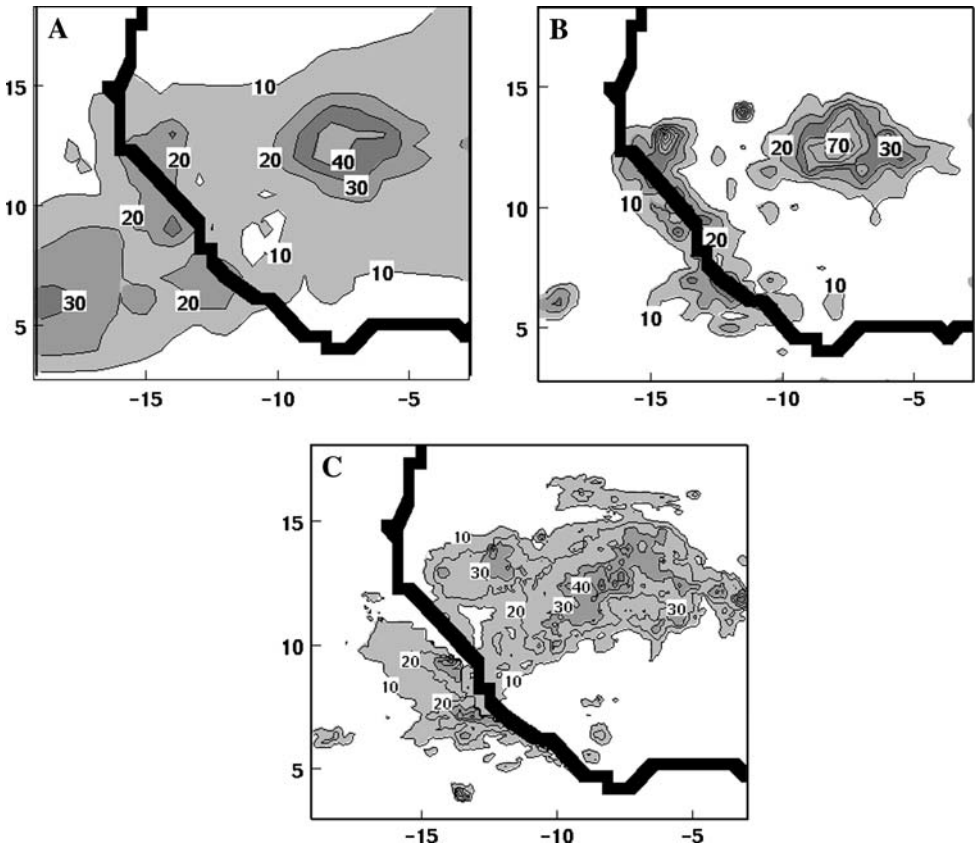

Fig. 4 Precipitation accumulations (mm) for September 10, 2006: **a** RM3 simulation, **b** TRMM estimates (Courtesy of NASA/DAAC/GSFC), and **c** FEWS estimates (Courtesy of NOAA/CPC)

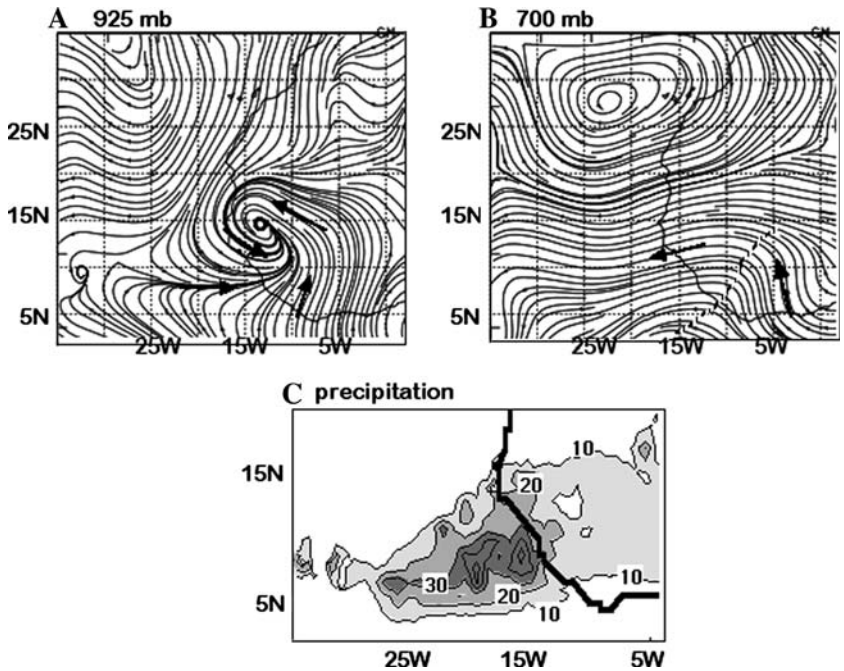

Fig. 5 Streamlines of RM3 simulated circulation for 00 UT at: **a** 925 mb, **b** 700 mb, and **c** RM3 simulated precipitation accumulations (mm), all for September 11, 2006

24 h precipitation accumulations for September 12 (Fig. 7b) validate the maximum along 21°W, while suggesting that the southern edge of the RM3 rain shield of light rainfall extends too far. SOP-3 TOGA (Tropical Ocean and Global Atmosphere) precipitation radar echoes recorded near Praia, Cape Verde (15°N, 23.5°W) at 12:30 UT on the same day (Fig. 7c) detected a solid area of precipitation southward from about 0.5° (50 km) south of the station. In fact, Praia itself and areas to the north remained echo free all that day (according to the NAMMA

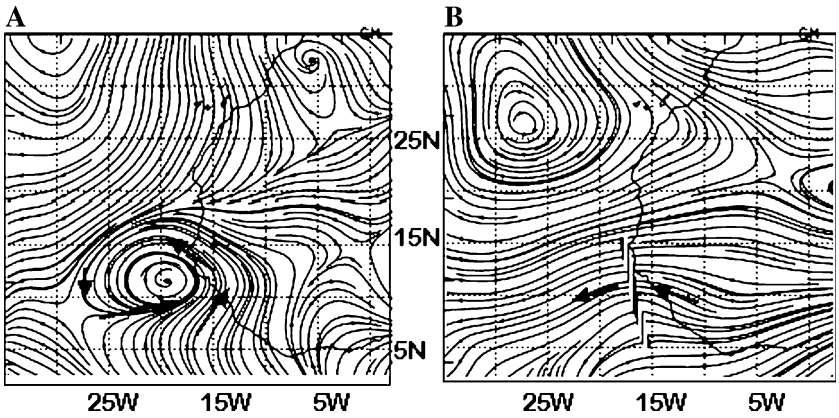

Fig. 6 Streamlines of RM3 simulated circulation for September 12, 2006 at 00 UT: **a** 925 mb, **b** 700 mb

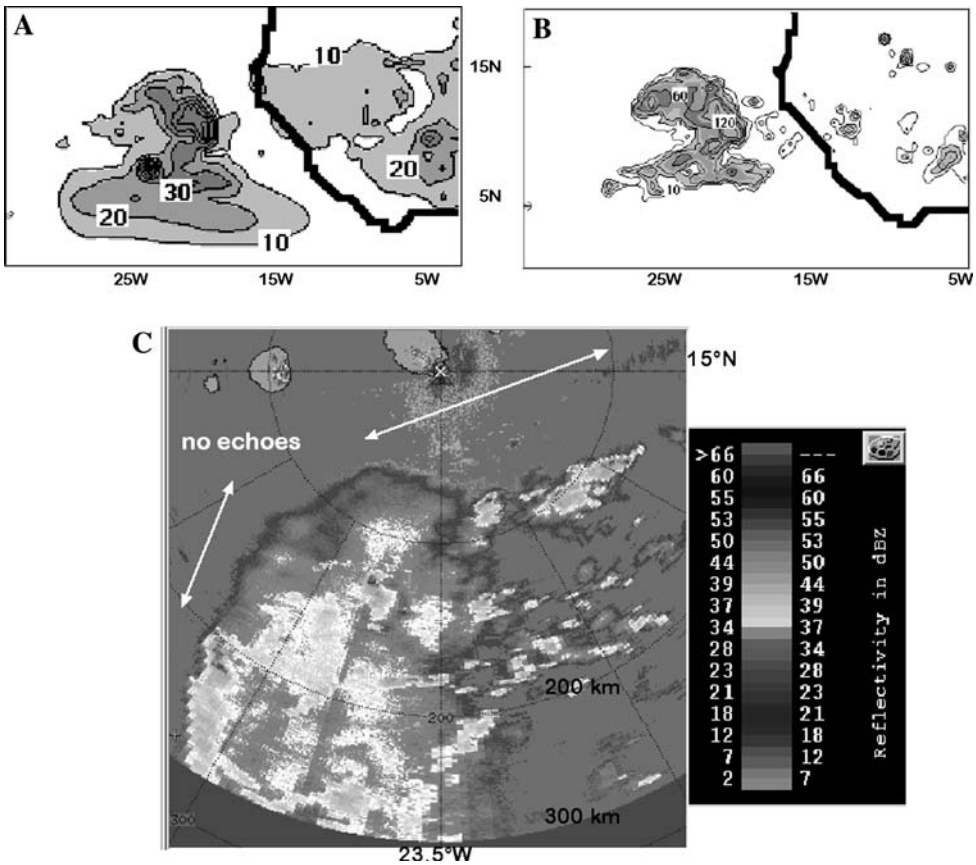

Fig. 7 **a** RM3 simulated precipitation accumulations (mm) for September 12, 2006, **b** TRMM estimated precipitation accumulations (mm) for September 12, 2006 (contours: 10, 20, 30, 60, 90, 120 mm) (Courtesy of NASA/DAAC/GSFC), and **c** precipitation radar echoes recorded near Praia, Cape Verde (15°N, 23.5°W) at 12:30 UT on September 12, 2006 (Courtesy of NAMMA/TOGA)

TOGA blog). The storm's passage brought wind shifts and humidity increases that can be discerned on time-altitude cross-sections of SOP-3 radiosonde observed winds and humidity at Praia (Schmidlin et al. 2007). While precipitation was detected by TOGA radar west of the trough from September 12, trough passage occurred early on September 13. These ground-based observations are entirely consistent with the RM3 simulation.

Figure 8a, b shows the 925 and 700 mb circulations, respectively, for 00 UT on September 13th. The positions of the 925 mb center on the three previous days are also indicated. The southward shift in the vortex trajectory after crossing the coastline is obvious. Most of the NE-SW oriented trough is now vertical and it has advanced some 5–8° further west in the last 24 h. The precipitation shield (Fig. 8c) wraps around the surface low from northwest to southwest to south. The extent of areas experiencing maximum rates has diminished since the previous 24 h period. Meanwhile, the next cyclonic vortex appears at 9°N, 2.5°W (Fig. 8a) with its associated precipitation maximum clearly visible over 8°N, 6°W (Fig. 8c).

WRF model simulation results are next considered and compared with the foregoing analysis. Figure 9a shows that the September 10, 00 UT position of the near-surface

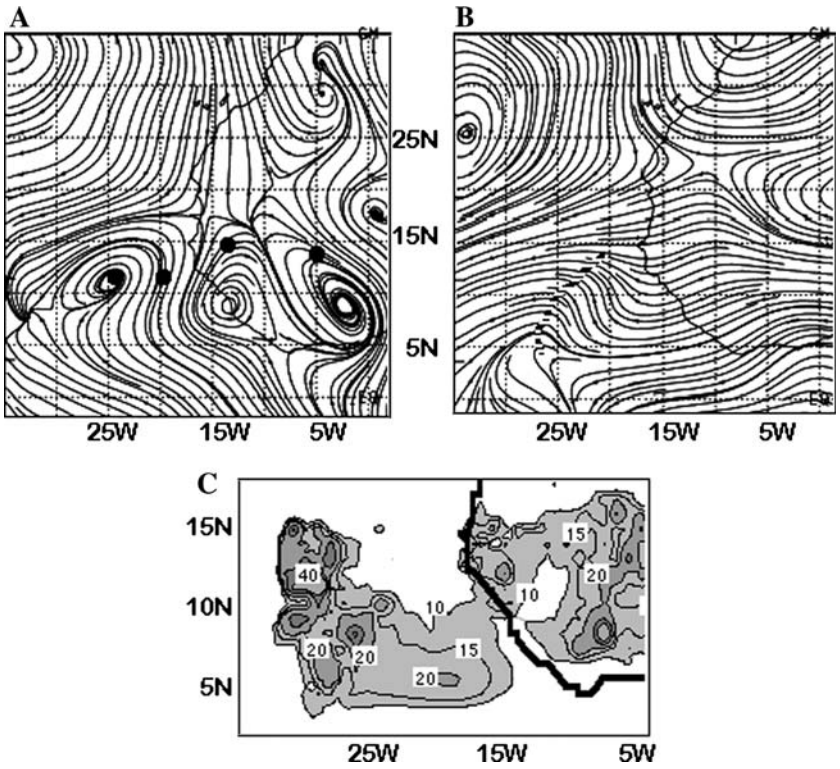

Fig. 8 Streamlines of RM3 simulated circulation for 00 UT for: **a** 925 mb, **b** 700 mb, and **c** RM3 simulated precipitation accumulations (mm), all for September 13, 2006. *Dots* in (**a**) indicate positions of the vortex center at 00 UT for each day, September 10–13

circulation cyclonic vortex in the WRF simulation was downstream (west) of the RM3 and NCPR2 solutions by some 7°. In fact it was even displaced westward of the corresponding FNL position (not shown). The WRF 700 mb trough (Fig. 9b) intersects the African coast at about 12.5°W, also some 7.5° west of the RM3 position. The WRF distribution of precipitation for September 10 (Fig. 9c) does not include the distinctive circular shaped maximum so prominent in Fig. 4. WRF rather features a zonal band of very heavy precipitation along the 925 mb convergence line at the intersection of 10°N with the coastline, which is southwest of the actual maximum. Moreover, WRF maximum 24 h accumulations, ranging from 200 to 348 mm are quite excessive compared to observational evidence (Fig. 4b, c).

By September 12, WRF has moved the 925 mb cyclone vortex to 14°N, 21°W (Fig. 10), very close to its RM3 and FNL positions. The associated 700 mb trough is directly over the surface system, but is much sharper than the corresponding RM3 interpretation, and judging by NCPR2 and FNL analyses, probably more realistic. WRF continues to exaggerate the area of heavy rainfall into September 11 (not shown), but accumulations are more reasonable for September 12. Figure 10c shows that WRF simulates a comma shaped precipitation signature, wrapped around the southeast and northeast sides of the 925 mb vortex. The pattern is similar to those shown in Fig. 7, but there are some noteworthy differences from the RM3 and TRMM configurations. For example, Cape Verde radar (Fig. 7c) and the NAMMA TOGA blog, indicate that the precipitation on September 12 probably did not reach as far north as 15°N, contrary to the WRF solution. In addition, although WRF rates are similar to observational evidence within the southwest tongue of the precipitation shield, the model fails to simulate the heavy precipitation along 21°W indicated by both the RM3 and TRMM (Fig. 7a, b).

4.2 Cumulus heating rates of RM3

Futyan and Del Genio (2007) showed that for mature large and deep convective systems TRMM precipitation radar reflectivity tends to be stronger in the lower troposphere over the eastern tropical Atlantic than over West Africa. High radar reflectivity indicates the presence of large hydrometeors. They ascribe the lower precipitation reflectivity within the 0–4 km layer over Africa to a stronger diurnal cycle and influx of dry air. These may combine to evaporate falling precipitation and to inhibit new condensation. The small diurnal cycle and high humidity above the ocean, on the other hand, create a more favorable environment for falling precipitation and new condensation. Cumulus heating rates (CHRs), which monitor condensation within moist convective plumes, should peak within the layers of high radar reflectivity, although the original condensation can sometimes be transported to

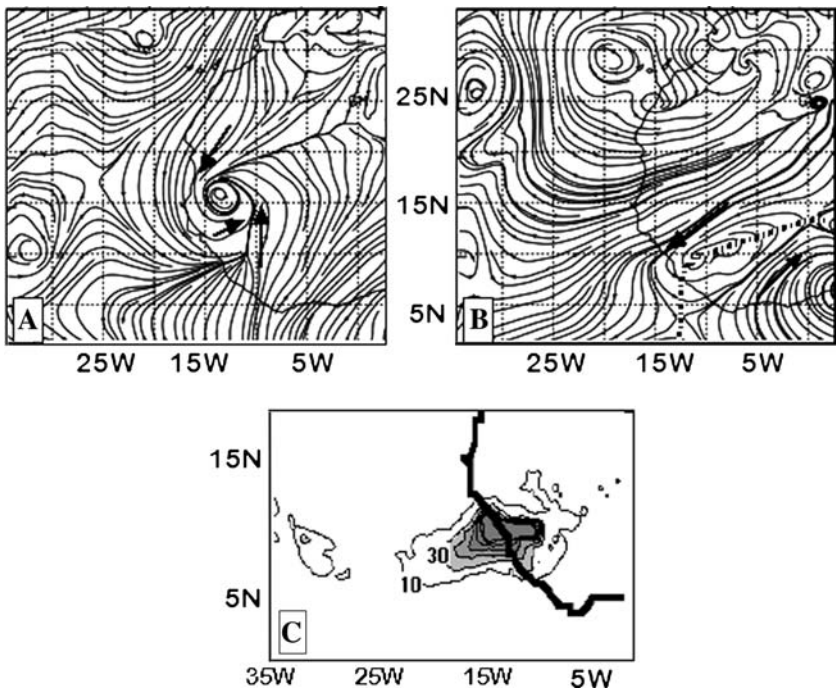

Fig. 9 **a** Streamlines of WRF simulated circulation at 925 mb for September 10, 2006 at 00 UT, **b** like (**a**) but for 700 mb, and **c** WRF 24 h precipitation accumulations (mm) for September 10, 2006. Contour interval is 20 mm

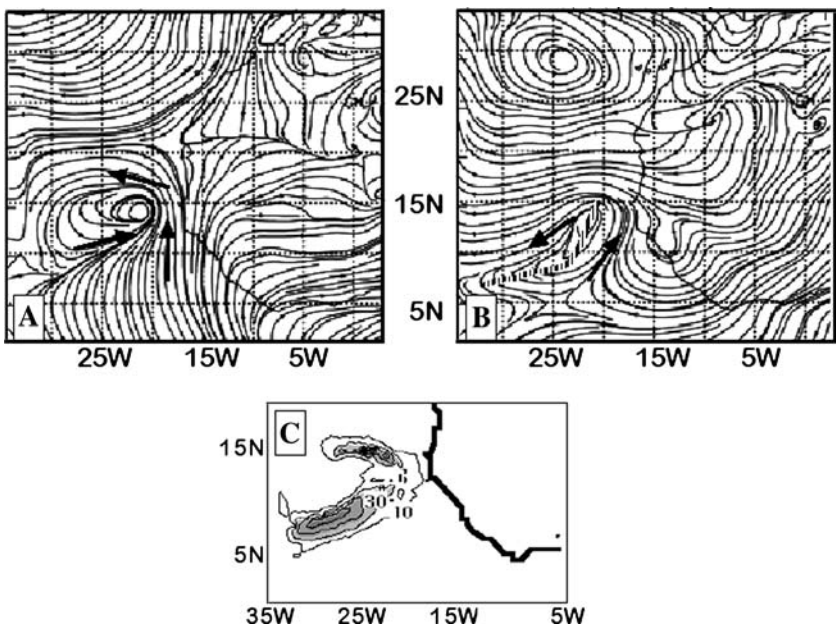

Fig. 10 **a** Streamlines of WRF simulated circulation at 925 mb for September 12, 2006 at 00 UT, **b** as in (**a**) but for 700 mb and **c** WRF precipitation accumulations (mm) for September 12, 2006. Contour interval: 20 mm

different levels. CHRs of the June–September 2003 climate over West Africa were previously shown for RM3 simulations at two vertical resolutions (Druyan et al. 2008).

Do AEWs experience noticeable changes in CHR profiles as they transfer from continent to ocean? The vertical profile of CHRs was monitored within the center of heaviest simulated precipitation following the movement of the pre-Helene disturbance over four successive days. Results refer to deep convection that spans a vertical interval of at least 400 mb. Figure 11a shows that within the center of heavy precipitation on September 10, an area bounded by 11–14°N, 5–10°W, there was one prominent peak at 477 mb.

Figure 11b shows how the profile of cumulus heating rates changed by the next day when the storm's heaviest precipitation was over the Atlantic (6–9°N, 13–20°W). This profile reflects the influences of latent and sensible heat fluxes during the transition from the continent to the warm ocean, and shows a very large spike at 967 mb, a secondary peak at 779 mb and the major peak at 528 mb.

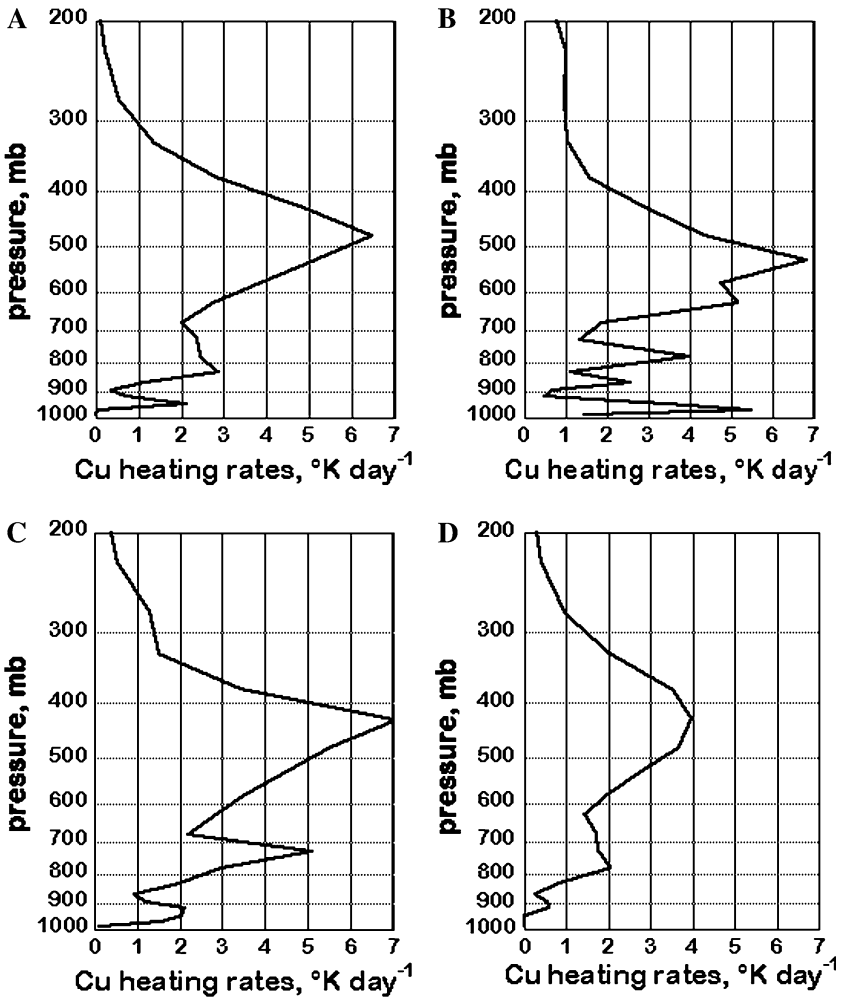

Fig. 11 Cumulus heating profiles (°K day^{-1} vs. mb) within deep convection, averaged over the designated areas: **a** 14°N, 5–10°W on September 10, 2006, **b** 6–9°N, 13–20°W on September 11, 2006, **c** 7–14°N, 20–25°W on September 12, 2006, and **d** 7–15°N, 28–32°W on September 13, 2006

Thus, the mid-tropospheric peak remains, but maxima are added in the lower troposphere. The profile of cumulus heating rates for September 12 (Fig. 11c) is taken within the heavy precipitation area, which is entirely over the ocean. Peaks of this profile are at 729 and 427 mb, and the lower one (at 729 mb) is more pronounced than on the previous 2 days. This indicates that, over the ocean, significant condensation occurs closer to the surface, owing to the improved moisture supply from enhanced upward latent heat flux. On September 13 CHRs that are computed for 7–15°N, 28–32°W (Fig. 11d) show one prominent peak of only 4°K day^{-1} at 427 mb. These results parallel the analysis of Futyan and Del Genio (2007) and suggest that the transition of the AEW to the maritime environment is accompanied by a lowering of the base of precipitating cumulus. They also provide evidence that the maritime environment provides more sustainable moist convection with concomitantly improved moisture supply to the AEW. Low- level cumulus heating enhances upward motion and therefore favors intensification of the existing storm.

4.3 AEW vertical structure of wind and geopotential height anomalies

4.3.1 September 10, 2006: 925 mb vortex at 14°N, 5°W

The vertical structure of circulation and geopotential height associated with the AEW is analyzed by means of zonal and meridional cross-sections. Meridional and zonal wind anomalies discussed in this section are computed as differences between simulated 00 UT values and September 2006 means. The anomalies show how the mean circulation is perturbed by the traversing AEW. Results from the current simulation are compared to the RM3 composite of seven AEWs over West Africa during the months of August and September of four different seasons, analyzed by Druyan et al. (2008). For the current results, the west to east transect of RM3 meridional wind anomalies (v_a) in Fig. 12a is along 12–13°N, which is close to the latitude of the 925 mb cyclonic vortex. Negative v_a on the west side represents northerly perturbations in circulation caused by

the cyclonic system and positive v_a represents southerlies, concentrated east of the low. Northerly anomalies extend throughout the troposphere with extreme values near 600 mb, but the meridional circulation is close to the September mean near the surface. The $v_a = 0$ contour marks the transition between anomalous northerly and southerly circulation. This transition, or trough, is well defined at all levels above 900 mb. Although southerly wind anomalies also extend throughout the troposphere, strong positive values are confined to a shallow layer below 800 mb. Moreover, results show a rather steep eastward tilt of the trough upward to the 700 mb level. Kiladis and Thorncroft (2008) found eastward tilts with altitude to be typical of AEWs over West Africa and consistent with baroclinic growth. It was previously shown that the 700 mb trough on September 10 was displaced eastward about 5° longitude from the surface low. Figure 12a resembles the corresponding cross-section of v_a from the RM3 composite analyzed by Druyan et al. (2008), except that in the composite southerly wind anomalies are strong also at 600 mb.

Figure 12b is a north–south transect of RM3 zonal wind anomalies (u_a) along 3–5°W through the near-surface cyclonic vortex. Westerly anomalies south of the low occupy most of the troposphere and are strongest at 600 mb. This matches the Druyan et al. (2008) composite, which also featured positive (westerly) wind anomalies south of the disturbance throughout a rather deep layer. North of the AEW easterly circulation is enhanced, especially in the upper troposphere. This enhancement of upper tropospheric easterlies departs somewhat from the structure of the composite wave of Druyan et al. (2008), which featured only a slight enhancement of easterlies north of the AEW, most prominently in the lower troposphere. The different result here is because the trough of the AEW of September 10, 2006 was tilted more to the northeast than the composite wave. The corresponding NCPR2 cross

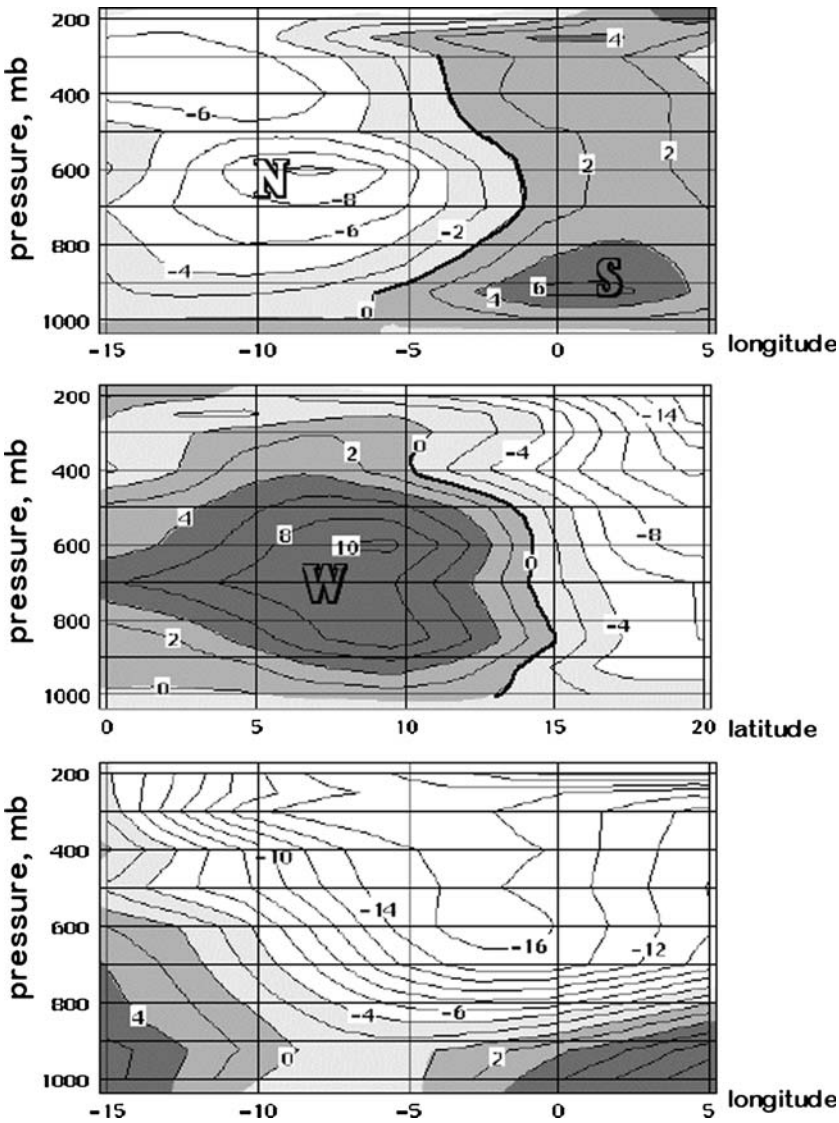

Fig. 12 September 10, 2006, 00 UT anomalies, relative to September 2006 means: **a** west–east transect of RM3 meridional wind anomalies (m s^{-1}), averaged over 12–13°N, **b** north–south transect of RM3 zonal wind anomalies (m s^{-1}), averaged over 3–5°W, and **c** west–east transect of RM3 geopotential height anomalies (m), averaged over 12–13°N

section (not shown) features a similar pattern of negative u_a, including acceleration of upper tropospheric easterlies at 20°N. The north–south orientation of the composite wave trough, on the other hand, limited the enhancement of easterlies north of the AEW. Thus, each AEW develops with its own anomalous characteristics. Figure 12c shows that the geopotential minimum caused by the AEW on September 10 was deepest in the mid-troposphere, also some 5° longitude east of the surface low.

4.3.2 September 12, 2006: 925 mb vortex at 12°N, 20°W

Figure 13a, b, c shows the RM3 simulated structure of the disturbance on September 12, when the cyclonic system was mostly over coastal Atlantic Ocean waters. The transect of v_a along 12–13°N (Fig. 13a) indicates that, unlike over land, northerly circulation anomalies west of the center reach the ocean surface, indicating intensification within the lower levels, although the most extreme values still occur at 600 mb. Southerly anomalies to the east are still strongest below 800 mb, and comparison of Fig. 13a to Fig. 12a shows that the lateral cyclonic shear of v_a is stronger in the lower troposphere on September 12 than on September 10. However, the axis separating northerlies and southerlies maintains a similar tilt on both days, so that the upper trough is still displaced eastward from the surface low. Figure 13b is a north–south transect of RM3 zonal wind anomalies along 17–20°W through the near-surface cyclonic vortex. There is evidence of the AEW's impact on zonal winds at most levels. The strongest westerly anomalies south of the low occur at 500–600 mb, compared with the 600–700 mb extreme over land 2 days earlier. To the north, the easterly anomalies, which extend throughout the troposphere, are most extreme at 400 mb (in agreement

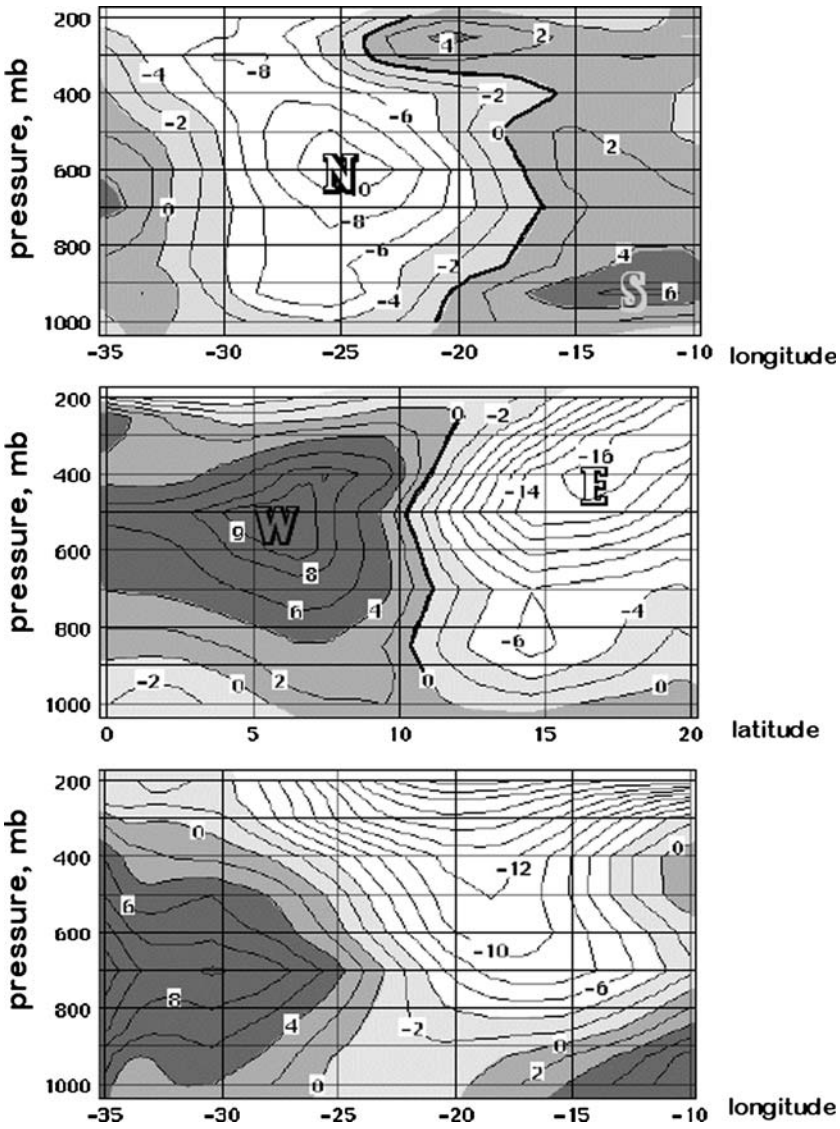

Fig. 13 September 12, 2006, 00 UT anomalies, relative to September 2006 means: **a** West–east transect of RM3 meridional wind anomalies (m s^{-1}), averaged over 12–13°N, **b** North–south transect of RM3 zonal wind anomalies (m s^{-1}), averaged over 17–20°W, and **c** West–east transect of RM3 geopotential height anomalies (m), averaged over 12–13°N

with NCPR2 data) and rather weak near the ocean surface. In fact, the zonal circulation near the ocean surface is minimally perturbed by the system. The acceleration of upper-level easterlies north of the AEW trough is more extreme within a deeper layer than when the system was over land (Fig. 12b) and the lateral cyclonic shear of u_a is also stronger on September 12 (Fig. 13b). Regarding the axis of minimum geopotential height anomalies associated with the low over the eastern tropical Atlantic: comparison of Fig. 13c to Fig. 12c shows that the eastward tilt of the trough with altitude between the ocean surface and 700 mb is not changed greatly in the transition from land to ocean. Kiladis and Thorncroft (2008) find that decreases in tilt during the transition are more usual and consistent with weakening baroclinicity, so maintenance of the tilt implies that this AEW is still fueled by baroclinic energy conversion. The geopotential height anomaly minimum is still more extreme in the mid-troposphere than near the surface and the east–west gradients are comparable with those over land. Negative geopotential height anomalies on September 12 are not as deep as they are on September 10 over land, but the westward ridge develops higher positive anomalies.

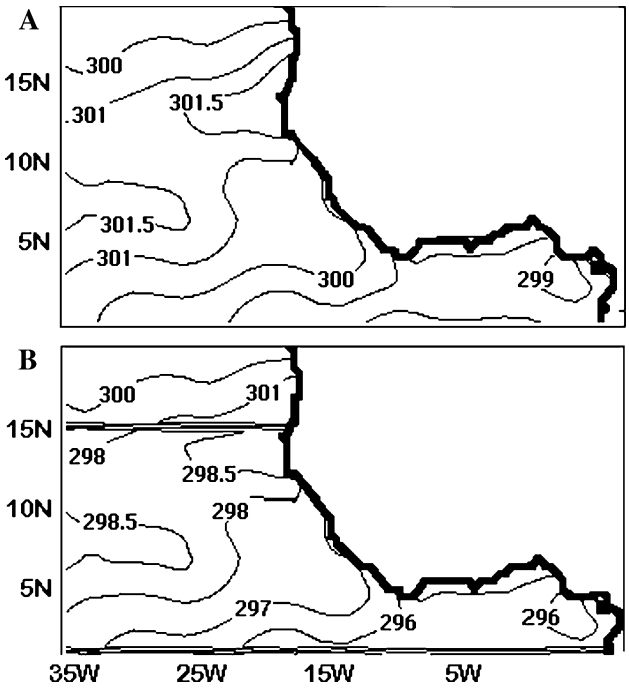

Fig. 14 SST lower boundary conditions on September 10–13, 2006: **a** control simulation and **b** c3.0 K simulation (°K)

5 SST anomaly experiments

The position of inter-tropical convergence zone (ITCZ) maximum convective activity over the Atlantic Ocean depends on SST gradients (Chiang et al. 2002), so daily rainfall rates are presumably sensitive to SST anomalies. Destabilizing warm water triggers convective precipitation and promotes upward water vapor flux that feeds the developing cumulus, while cold SST anomalies inhibit moist convection. Given the importance of moist convection to a tropical storm's energy budget, what impact do SST anomalies have on a developing AEW over the eastern Atlantic? Several simulation experiments are conducted to evaluate the sensitivity of the pre-Helene AEW and associated precipitation to the magnitude of the SST maximum in the tropical North Atlantic near Africa. The RM3 simulation, August 15–September 30, is repeated twice with cold SST anomalies imposed within the swath of the normal SST maximum in the tropical eastern North Atlantic Ocean. In experiment *c1.5K*, 1.5°K is subtracted at every time step from all SSTs within the swath 0–15°N, from the western boundary (35°W) eastward to the African coast. In experiment *c3.0K*, 3.0°K is subtracted at every time step from all SSTs within the same swath. A 3.0°K anomaly of the monthly mean SST is near the high end of naturally occurring events over broad tropical ocean areas. Figure 14 shows the control and *c3.0K* SST distributions, respectively, for September 10–13, 2006. SSTs for the *c1.5K* experiment are intermediary between Fig. 14a and b. Maximum Atlantic Ocean SSTs in the control are accordingly reduced from 301.5 to 300°K or 298.5°K and from 298.5 to 297°K or 295.5°K in the Gulf of Guinea.

The circulation on each day during September 10–13 at 925 and 700 mb for each experiment is compared. Neither cold SST anomaly experiment shows any noticeable impact on streamline patterns, including the positions of the near-surface vortex and mid-tropospheric trough. In fact, simulated u and v components are hardly changed by the SST anomalies, even in the *c3.0K* case, until September 25. These results emphasize the strong control that the lateral boundary conditions, which are identical in all experiments, exercise on the simulated circulation throughout the domain.

The time-latitude Hovmöller plot of daily precipitation averaged between 30 and 17°W for the control simulation agrees reasonably well with TRMM observational evidence over the Atlantic sector (Fig. 15) where the ITCZ rain band hovers over 7–8°N during the month of September 2006. The space–time correlation between the data shown in the two panels of Fig. 15 is 0.64, which is significant to the 99% confidence level. Several precipitation events with heavy rainfall north of 10°N are notable. For example, the September 12th storm produces precipitation as far north as 16°N and it features a center of large-scale upward motion along a line through 12°N, 25°W to 10°N, 15°W (Fig. 16). Figure 17a shows the *c1.5K* minus control precipitation differences for the latitude-time Hovmöller distribution.

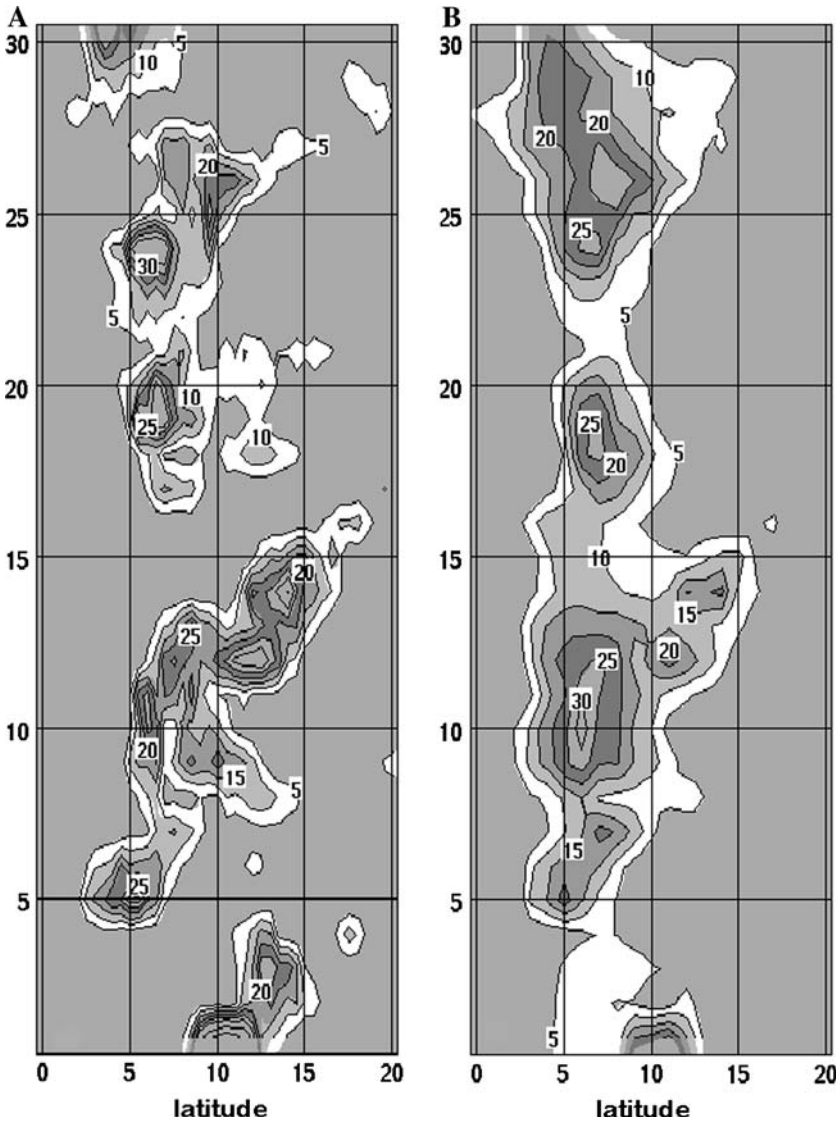

Fig. 15 Hovmöller time–latitude distributions of daily rainfall, September 1–30, averaged between 30 and 17°W. **a** TRMM and **b** RM3 control simulation

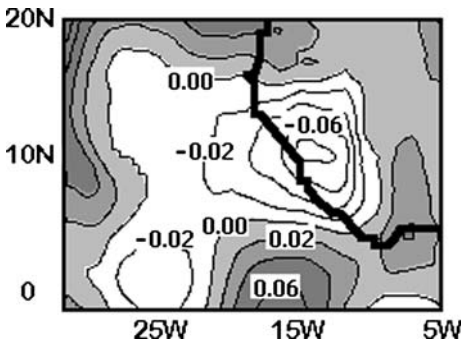

Fig. 16 RM3 simulated vertical motion (omega, pascals s^{-1}) at 700 mb for September 12, 2006. Upward motion is indicated by white areas

The impact of the SST anomalies is to diminish precipitation within the swath at 5–8°N, but to enhance rainfall to the north until about September 17. Subsequently, there is only one additional occurrence of enhancement, at 11–12°N on September 25–26. The swath of precipitation deficits resulting from the *c1.5K* SST anomalies broadens toward the end of the month, enveloping the entire ITCZ rain band during the last week in September, with extreme deficits of as much as -22 mm day^{-1}. Figure 17b shows the *c3.0K* minus control precipitation differences for the latitude-time Hovmöller distribution, which features the same dipole of negative and positive impacts as the *c1.5K* case. However, the more extreme SST anomalies produce more extreme precipitation deficits along 5–8°N during most of the month and the same or slightly greater precipitation enhancement north of 9°N. Negative impacts after September 23 are similar for the two experiments. Figure 18 shows that on September 12 the *c3.0K* SST anomalies enhance precipitation rates within nearly the entire northern portion of the AEW precipitation shield, including the area of the near-surface vortex (Fig. 6a),

overlapping the area of 700 mb upward vertical motion (Fig. 16). In contrast, the band of reduced precipitation corresponds to southerly 925 mb circulation south of the storm and to mostly subsidence or weak large-scale vertical motion (at 700 mb).

Figure 19a shows the RM3 control simulation temperature distribution at 925 mb on September 12, 2006 (average of 00, 06, 12, and 18 UT). The axis of maximum values over the eastern Atlantic Ocean is along approximately 22°N. Figure 19b shows that the maximum SSTs in the control simulation occur some 5–10° south of the 925 mb temperature maximum. The difference between these two fields (Fig. 19c) represents the mean vertical temperature lapse rate from ocean surface to 925 mb. The disparity in the latitudes of the maxima creates a temperature inversion at 22°N in contrast to a very steep lapse rate between 3 and 10°N, which includes the latitude of the ITCZ rain band. Figure 19d shows the same vertical lapse rates for the *c3.0K* experiment. The lapse rates for the *c1.5K* experiment (not shown) are intermediary between Fig. 19c and d. Stabilization of the lapse rates (less extreme negative values) in the *c1.5K* and *c3.0K* experiments is undoubtedly responsible for much of the negative impacts on simulated precipitation south of 9°N. Between 9 and

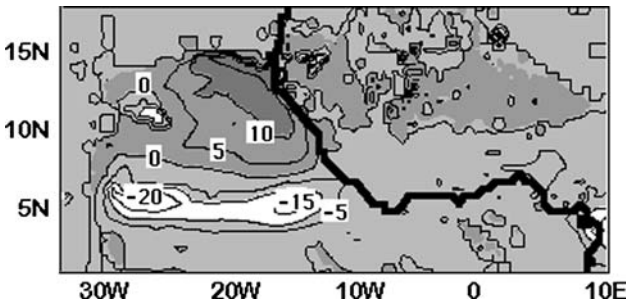

Fig. 18 The *c3.0K* simulation impact on precipitation (mm) on September 12, 2006

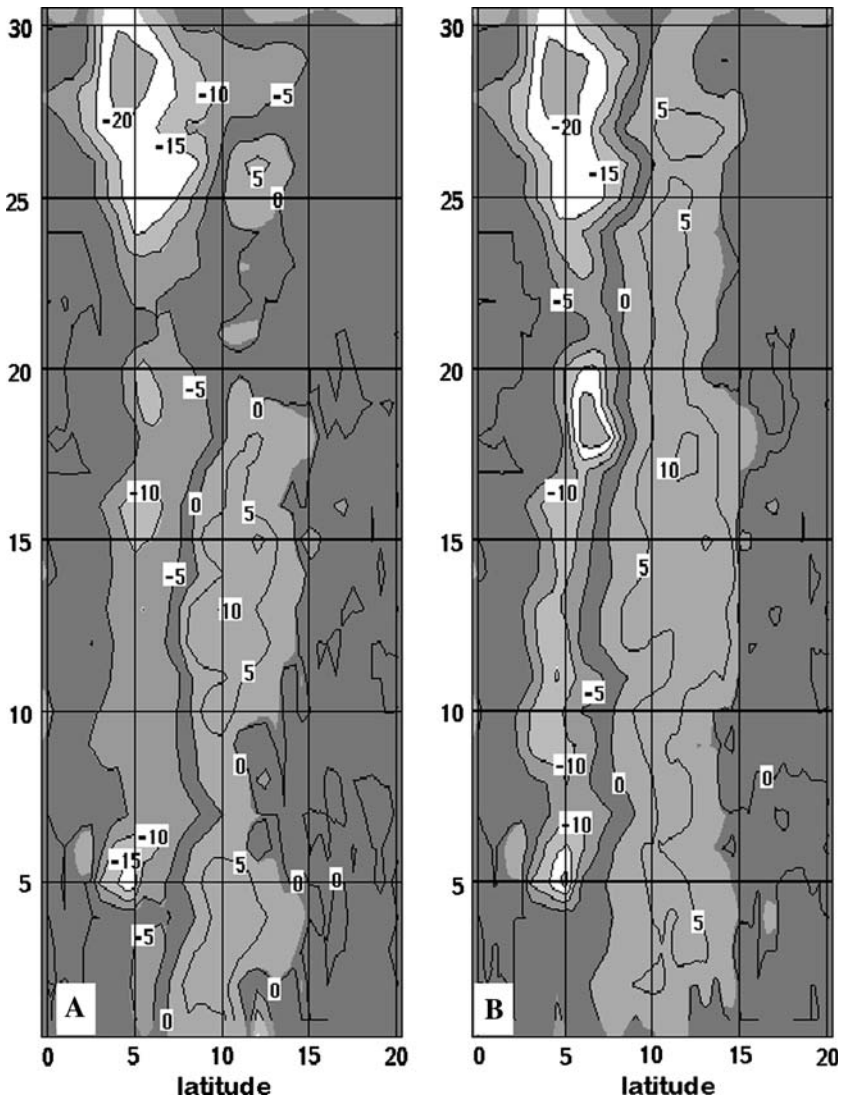

Fig. 17 Hovmöller time–latitude distributions of differences in daily rainfall, September 1–30, **a** *c1.5K* experiment minus RM3 control and **b** *c3.0K* experiment minus RM3 control, averaged between 30 and 17°W

15°N the more moderate lapse rates present in the control become closer to isothermal in the cold anomaly experiments. However, this latitude band experiences precipitation events primarily associated with large-scale uplift, often from transient cyclonic systems, and less as a consequence of vertical thermal instability. The cold SST anomaly simulations generate enhanced precipitation rates north of 9°N due to a richer supply of moisture, as shown in the example for September 12, below.

Lower SSTs in the two simulation experiments inhibit convective rainfall south of 8°N. The reason for the enhancement of precipitation north of 9°N in both experiments is less obvious. The strong enhancement of precipitation during September 11–14 (Fig. 17) coincides with strong large-scale upward motion associated with the AEW discussed above, which spreads precipitation to higher latitudes. Results indicate that less frequent or diminished convective rainfall above the colder SSTs along 5–8°N allows more (surviving) moisture to be supplied to areas of large scale convergence and uplift to the north, such as from transient storms. For example, on September 12, the mean northward specific humidity flux crossing 8°N (between 15 and 25°W) at 925 mb is 94.5 g kg^{-1} m s^{-1} for the *c3.0K* case and only 85.9 g kg^{-1} m s^{-1} for the RM3 control simulation, and the meridional specific humidity convergence between 8 and 14°N is 14.3 g kg^{-1} m s^{-1} for *c3.0K* versus 12.0 g kg^{-1} m s^{-1} for the control. This higher rate of moisture convergence in the *c3.0K* experiment enhances precipitation rates within the 9–15°N swath.

The impact of the imposed cold SST anomalies on surface latent heat flux (LHF) is evaluated for September 11–13, the days that the storm traversed the eastern Atlantic within the RM3 domain. The reduction of the 3-day mean LHF due to the *c3.0K* anomalies is between 5 and 10% of the control values (6–10 Wm^{-2}) over most of the anomaly area, increasing to about 13% near the Equator where surface wind speeds are stronger (not shown). Decreases in sensible heat fluxes are only 1–3 Wm^{-2}. Accordingly, some of the reduction in simulated precipitation in the cold SST anomaly experiments is apparently attributable to slightly lower LHF from the ocean surface.

Cumulus heating rate (CHR) profiles on September 11–13 for *c1.5K* experiment deep and shallow moist convection within precipitation areas (same areas as in CHR diagnostics described above) are not weaker than corresponding control CHR (not shown). This is consistent with the mixed response of both reduction and enhancement of precipitation, discussed above. However, CHR peaks consistently have lower amplitudes in the *c3.0K* experiment during this period when the developing storm, the future 'Helene,' traverses the region. Figure 20 shows the profiles of CHR on September 12th within the control precipitation area 7–14°N, 20–25°W (Fig. 7a). In this example, the main CHR peak at 427 mb in the *c3.0K* experiment is only 72% of the peak simulated by the control and the lower *c3.0K* CHR peak at 729 mb is only 63% of the control value. These reductions in CHR peaks relate to deep convection, which is somewhat inhibited by the experimental cold SST anomalies. The CHR reductions occur despite the enhancement of large-scale precipitation within the cyclonic system (Fig. 18). Note that cumulus heating is positive wherever convection results in condensation, even when precipitation does not reach the ground or ocean surface. Reductions in CHR indicate that the cyclonic system receives less latent heat to fuel the intensification of the AEW in the *c3.0K* case.

A warm SST simulation experiment imposes +1.5°K differences in tropical North Atlantic SSTs (*w1.5K*), as before between 0 and 15°N. Results of this simulation (not shown) feature broad increases in daily precipitation

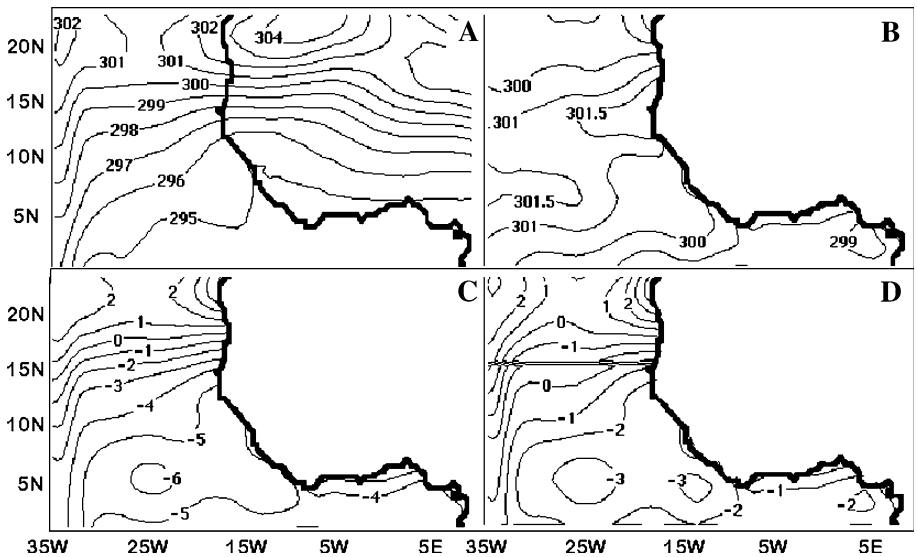

Fig. 19 **a** T 925 mb (September 12) control simulation, **b** SST (September 10–13) control simulation, **c** T 925 mb (September 12) minus SST (September 10–13) control simulation, and **d** T 925 mb (September 12) minus SST (September 10–13) *c3.0K* simulation

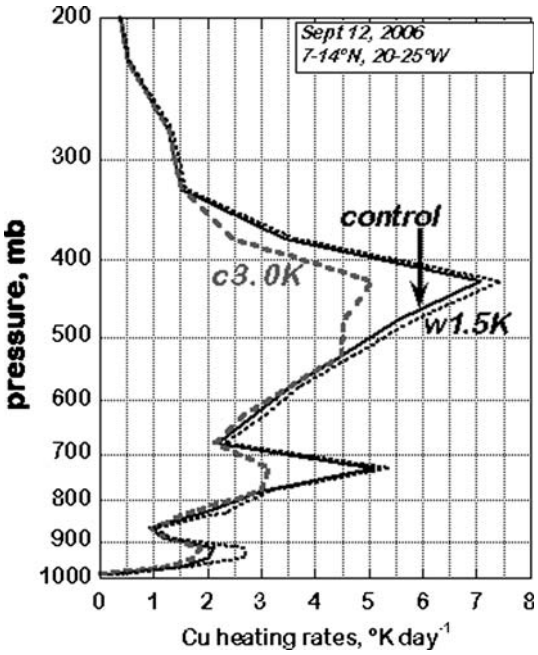

Fig. 20 Vertical profiles of cumulus heating rates (°K day^{-1} vs. mb) for control, *c3.0K* and *w1.5K* RM3 simulations on September 12, 2006, averaged over the area 7–14°N, 20–25°W

between 0 and 10°N until September 24, followed by negative impacts. The largest enhancement occurs near the Equator during September 9–20 and it relates to the decrease in thermal vertical stability imposed by the SST changes. In addition, the warm SST perturbations have a small impact on CHR, for example on September 12 within the rainy area associated with the pre-Helene AEW (7–14°N, 20–25°W, see Fig. 20). All three *w1.5K* CHR peaks occur at the same levels as in the control, and all three indicate slightly higher heating rates than the control values. The strongest impact is an increase of about 33% at 917 mb indicating an improved supply of latent heating to the developing cyclone.

6 Conclusion

The evolution of the meteorological regime over West Africa and the southeastern North Atlantic during the AMMA Special Observing Period #3 (SOP-3, September 2006) is studied in simulation results from two regional climate models, both of which downscale global analyses to a 0.5° grid. The RM3 is forced by synchronous lateral boundary conditions (LBCs) from NCEP reanalysis II from August 15 to September 30, 2006 and WRF is forced by LBCs from GFS FNL analyses August 1 to September 30, 2006. At the time of the study NCAR provided WRF modules for creating LBCs from GFS data and not from NCPR2. Several RM3 studies of the WAM during other seasons have been previously been published (Druyan et al. 2006, 2008), while WRF applications for this region have been largely untested until now.

At least seven African easterly waves (AEWs) leave West Africa and move out over the southeastern North Atlantic Ocean during the SOP-3. Spectral analysis and wavelets of 700 mb meridional wind detect peaks for roughly 3–4-day periods, indicative of AEWs, but the peaks are higher over West Africa than over the adjacent Atlantic. RM3 results, confirmed by TRMM estimates, indicate that the heaviest westward propagating precipitation from among these AEWs is associated with the precursor to Hurricane Helene, which first attains tropical depression strength on September 12. Wavelet analysis, in fact, implies that the only statistically significant periodic behavior of *v7* during the entire month is during a 10-day interval that includes this storm's passage. The current study examines, in particular detail, RM3 simulations of this system as it moves across West Africa and out over the southeastern North Atlantic Ocean during September 10–13, 2006. Some features of the parallel WRF simulation are also highlighted. The disturbance is manifest by a 700 mb trough and a closed near-surface cyclonic vortex imbedded under the 700 mb northeasterlies west of the trough. This AEW causes cyclonic perturbations to the mean circulation and mean geopotential height fields that are strongest in the mid-troposphere. Once over the Atlantic, circulation anomalies caused by the AEW are evident throughout the troposphere, including intensified cyclonic circulation near 400–500 mb and near the ocean surface. Vertical profiles of cumulus heating rates from deep moist convection within the storm's precipitation shield show mid-tropospheric peaks of about 6°K day^{-1}, but peaks are added in the lower troposphere after the storm moves out over the Atlantic. Thus, the September 12th peak of 5°K day^{-1} at 729 mb, due to higher upward latent heat flux directly over the ocean, implies the lowering of cumulus bases as the system takes on maritime characteristics. Since the maritime environment improves the sustainability of moist convection, the transition from continent to ocean increases the supply of latent heat energy, contributing to the intensification of the AEW.

Only one of six WRF model configurations that were tried gives reasonable results. In the best WRF results (reported here), the cyclonic system over West Africa on September 10 is displaced some 5–10° downstream of its more probable position (based on observational evidence), although the validation improves once the storm enters the Atlantic. WRF 24-h precipitation accumulations associated with the continental phase of the storm are exaggerated, but accumulations are simulated more realistically over the southeastern North Atlantic Ocean. It is not possible to differentiate which aspects of the WRF simulation might

be attributable to the quality (or shortcomings) of the FNL forcing used for LBCs, as opposed to WRF model physics.

RM3 daily precipitation patterns are correlated in space and time with corresponding TRMM estimates, suggesting that the RM3 storm structure is realistic. Over land on September 10, a symmetrical mesoscale convective system develops under the western flank of the 700 mb trough, slightly southwest of the near-surface cyclonic center. As the AEW approached the Atlantic coast, the heaviest precipitation shifts southward, concentrating along lines of low level circulation convergence associated with the ITCZ. As it crosses the coast of Africa into the Atlantic, the near-surface cyclonic center also moves to a more southerly trajectory. By September 13 it slows enough to eventually become situated directly under the 700 mb trough. Results suggest that the near-surface cyclonic vortex was drawn toward the maritime area of greatest moist convective activity.

The analysis finds that convective precipitation over the southeastern North Atlantic between 5 and 8°N is related to thermal vertical instability above the warmest SSTs. Large-scale upward vertical motion north of 9°N, often associated with transient cyclonic disturbances, contributes to rainfall north of the mean ITCZ. Experiments with cold SST perturbations (−1.5°K and −3.0°K) yield lower rates of convective rainfall within the 5–8°N swath, but lead to an enhancement of large-scale precipitation north of 9°N. Diagnostics show that lower precipitation within the ITCZ allows more moisture to be advected northward into the storm-related precipitation shield. Cumulus heating rate peaks within the (pre-Helene) tropical depression rain shield are reduced in the −3°K SST perturbation experiment by about 30%. The prescribed SST perturbations do not, however, have much impact on geopotential height or circulation, which is apparently constrained by the LBCs used in all the simulations. A parallel experiment with +1.5°K SST perturbations also does not show any impact on geopotential heights or the trajectory of the pre-Helene storm. The higher SSTs do, however, enhance convective rainfall near 8°N by decreasing vertical thermal stability in the lower troposphere. Concomitant with the precipitation enhancement, the *w1.5K* experiment records a small increase in cumulus heating rates of deep convection close to the ocean surface.

These conclusions represent the results of a case study of one particular month's climate. Similarly, the trajectory and structure of one particular cyclonic disturbance are described. This storm was the precursor to Tropical Storm Helene, which eventually became Hurricane Helene. Results provide insight into the characteristics and behavior of such storms, even though the full context of the findings will only be apparent after the sampling is increased by examining many more simulations.

Acknowledgments This research was supported by National Science Foundation grant ATM-0652518, National Aeronautics and Space Administration (NAMMA) grant NNX07A193G, and by the National Aeronautics and Space Administration Climate and Earth Observing System Program. E. Noble is a Fellow of the National Aeronautics and Space Administration Graduate Student Researchers Program. Helpful discussion about cumulus heating rate profiles with Dr. A. Del Genio is acknowledged. We gratefully acknowledge assistance from the WRF help desk at the National Center for Atmospheric Research and helpful consultations concerning WRF with Dr. Jimy Dudhia. TRMM data used in this study were acquired using the GES-DISC Interactive Online Visualization and Analysis Infrastructure (Giovanni) as part of the NASA's Goddard Earth Sciences (GES) Data and Information Services Center (DISC). NCEP reanalysis II data used in this study were obtained on-line from the National Oceanographic and Atmospheric Agency/Earth System Research Laboratory (Physical Sciences Division). FEWS data sets were created at the National Oceanographic and Atmospheric Agency Climate Prediction Center and made available on-line by the International Research Institute for Climate Prediction of Columbia University.

References

Brown D (2006) Tropical cyclone report, Hurricane Helene (AL082006). National Hurricane Center, NOAA, Miami, FL, p 12

Chen F, Dudhia J (2001) Coupling an advanced land-surface/hydrology model with the Penn State/NCAR MM5 modeling system. Part I: model description and implementation. Mon Wea Rev 129:569–585

Chiang JCH, Kushnir Y, Giannini A (2002) Deconstructing Atlantic ITCZ variability: influence of the local cross-equatorial SST gradient, and remote forcing from the eastern equatorial Pacific. J Geophys Res 107(D1):4004. doi:10.1029/2000JD000307

Chou M-D, Suarez MJ (1994) An efficient thermal infrared radiation parameterization for use in general circulation models. NASA Tech Memo 104606 3:85

Del Genio A, Yao M-S (1993) Efficient cumulus parameterization for long-term climate studies. The GISS scheme. In: Emanuel K, Raymond D (eds) Cumulus parameterization, vol 24. American Meteorology Society Monograph Series, Boston, pp 181–184

Del Genio A, Yao M-S, Kovari W, Lo K-W (1996) A prognostic cloud water parameterization for global climate models. J Clim 9:270–304

Diedhiou A, Janicot S, Viltard A, de Felice P, Laurent H (1999) Easterly wave regimes and associated convection over West Africa and tropical Atlantic: results from NCEP/NCAR and ECMWF reanalyses. Clim Dyn 15:795–822

Druyan L, Fulakeza M (2005) Mesoscale climate analysis over West Africa. CLIVAR Exch 10(20):34–35

Druyan L, Fulakeza M, Lonergan P (2006) Mesoscale analyses of West African summer climate: focus on wave disturbances. Clim Dyn 27:459–481

Druyan L, Fulakeza M, Lonergan P (2008) The impact of vertical resolution on regional model simulation of the west African summer monsoon. Int J Climatol 28:1293–1314. doi:10.1002/joc.1636

Fritsch M, Carbone R (2004) Improving quantitative precipitation forecasts in the warm season. Bull Am Meteorol Soc 85:955–965

Futyan J, Del Genio A (2007) Deep convective system evolution over Africa and the tropical Atlantic. J Clim 20:5041–5060. doi:10.1175/JCLI4297.1

Hansen J et al (2002) Climate forcings in Goddard Institute for Space Studies SI2000 simulations. JGR 107:4347. doi:10.1029/200IJD001143

Kain, JS, Fritsch JM (1993) Convective parameterization for mesoscale models: The Kain-Fritcsh scheme. In: Emanuel KA, Raymond, DJ (eds) The representation of cumulus convection in numerical models. American Meteorology Society, p 246

Kanamitsu M, Ebisuzaki W, Woollen J, Yang SK, Hnilo JJ, Fiorino M, Potter GL (2002) NCEP-DOE AMIP-II reanalysis (R-2). Bull Am Meteorol Soc 83:1631–1643

Kiladis G, Thorncroft C (2008) Three-dimensional structure of easterly wave disturbances over Africa and tropical North Atlantic. 20th conference on climate variability and change, New Orleans. http://ams.confex.com/ams/88Annual/techprogram/paper_128178.htm. Accessed 21 Jan 2008

Mlawer EJ, Taubman SJ, Brown PD, Iacono MJ, Clough SA (1997) Radiative transfer for inhomogeneous atmosphere: RRTM, a validated correlated-k model for the long- wave. J Geophys Res 102(D14):16663–16682

Redelsperger JL, Thorncroft CD, Diedhiou A, Lebel T, Parker DJ, Polcher J (2006) African monsoon multidisciplinary analysis: An international research project and field campaign. Bull Am Meteorol Soc 87:1739–1746

Reed R, Klinker E, Hollingsworth A (1988) The structure and characteristics of African easterly wave disturbances as determined from the ECMWF operational analysis/forecast system. Meteorol Atmos Phys 38:22–33

Rosenzweig C, Abramopoulos F (1997) Land-surface model development for the GISS GCM. J Clim 10:2040–2054

Schmidlin FJ, Morrison BJ, Northam ET, Gerlach J (2007) Detailed observations of five African Easterly waves during NAMMA. Ppt presentation, NAMMA Science Team Meeting. Workshop, Baltimore, MD, May 2007

Skamarock WC et al (2005) A description of the advanced research WRF version 2. NCAR technical note, June 2005, Revised January 2005

Thorncroft C, Hodges K (2001) African easterly wave variability and its relationship to Atlantic tropical cyclone activity. J Clim 14:1166–1179